Supplementary Information

Cryo-ultramicrotomy enables TEM characterization of global lithium/polymer interface†

Xuedong Zhang[1], Ziang Guo[2], Xin Li[2], Qiunan Liu[3], Huan Hu[1], Fangyuan Li[2], Qiao Huang[1], Liqiang Zhang[2,*], Yongfu Tang[2,*], Jianyu Huang[1,2,*]

1, School of Materials Science and Engineering, Xiangtan University, Xiangtan, Hunan 411105, P. R. China.

2, Clean Nano Energy Center, State Key Laboratory of Metastable Materials Science and Technology, Yanshan University, Qinhuangdao 066004, P. R. China.

3, SANKEN (The Institute of Scientific and Industrial Research), Osaka University Mihogaoka 8-1, Ibaraki, Osaka 567-0047, Japan

Corresponding Author

*Correspondence to: jyhuang8@hotmail.com; tangyongfu@ysu.edu.cn; lqzhang@ysu.edu.cn.

Supplementary Notes

Notes S1: As the sample consists of both lithium and polymer mediums, a significant mechanical strength mismatch exists between these mediums. Polymers exhibit higher hardness at low temperatures, while lithium metal is relatively soft and prone to creep even at low temperatures. Experimental evaluations were conducted through direct knife-edge cutting of both lithium and polymer, as illustrated in Fig. S1b, c. When the blade directly cut through lithium metal, the inherent creep characteristics lead to piling up of lithium at the blade edge, ruining the thin sections. In contrast, cutting polymer with the blade produces consistent thin sections owing to its higher and uniform hardness. Hence, meticulous sample preparation involved removing lithium from one electrode so that when the blade advanced, it passed the SPE first, then the lithium metal electrode. This ensured lithium creep does not ruin the thin sections.

Notes S2: The slicing procedure inherently introduces compressive strain along the cutting direction and cutting artifacts[1]. In the case of Li-SPE thin sections with thicknesses below 100 nm, prepared specimens experienced approximately 46% compressive strain (slice area: 130 × 130 μm²; individual Li-SPE thin section area: 130 × 60 μm²). It is worth noting that even conventional cryo-sectioning embedding agents, such as glass or resin samples, exhibit compression variations of about 30-60%[1]. This issue can be mitigated through strategies like adopting an oscillating diamond knife[2]. Moreover, these cutting defects do not disrupt the internal structure of the section but primarily influencing material extrusion and thin section thickness increment. They exert minimal influence on the central focus of this research, which pertains to the chemical interplay between lithium and SPE.

Supplementary Figures

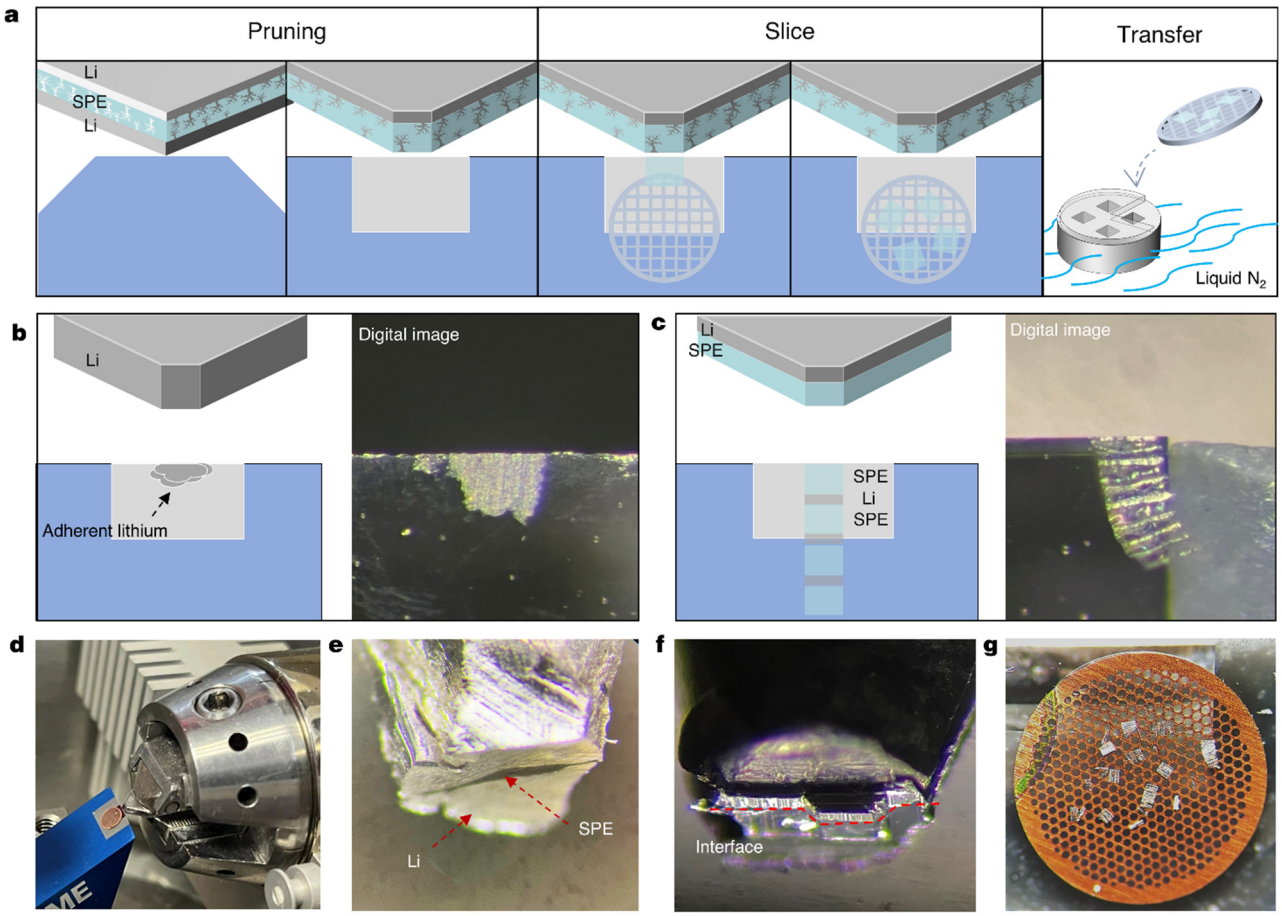

Fig. S1 | Schematic diagram of ultra-thin sections. a, Schematic of the sequential steps in the slicing procedure. The comprehensive slicing process encompasses sample contour refinement, sectioning, and relocation. To begin with, one side of the lithium metal was removed using a trapezoidal trimming tool, thus retaining the PEO-Li interface. Subsequently, the actual sectioning was performed through a diamond knife, and the obtained sections were meticulously transferred onto a TEM grid employing a delicate brush. Ultimately, the grid housing the sections was transferred to a cryogenic sample holder and stored under liquid nitrogen conditions; **b,** Schematic and experiment showing piling up of lithium along the blade surface when cutting lithium. c, when the blade cut the SPE first, then lithium metal, the lithium piling-up problem was mitigated; **d,** digital photographs during the sectioning process; **e**, untrimmed specimen showing SPEs as black areas and lithium metal as silver-white regions; **f**, trimmed Li-PEO interface, with SPEs below and lithium metal; **g**, thin sections placed on a TEM grid.

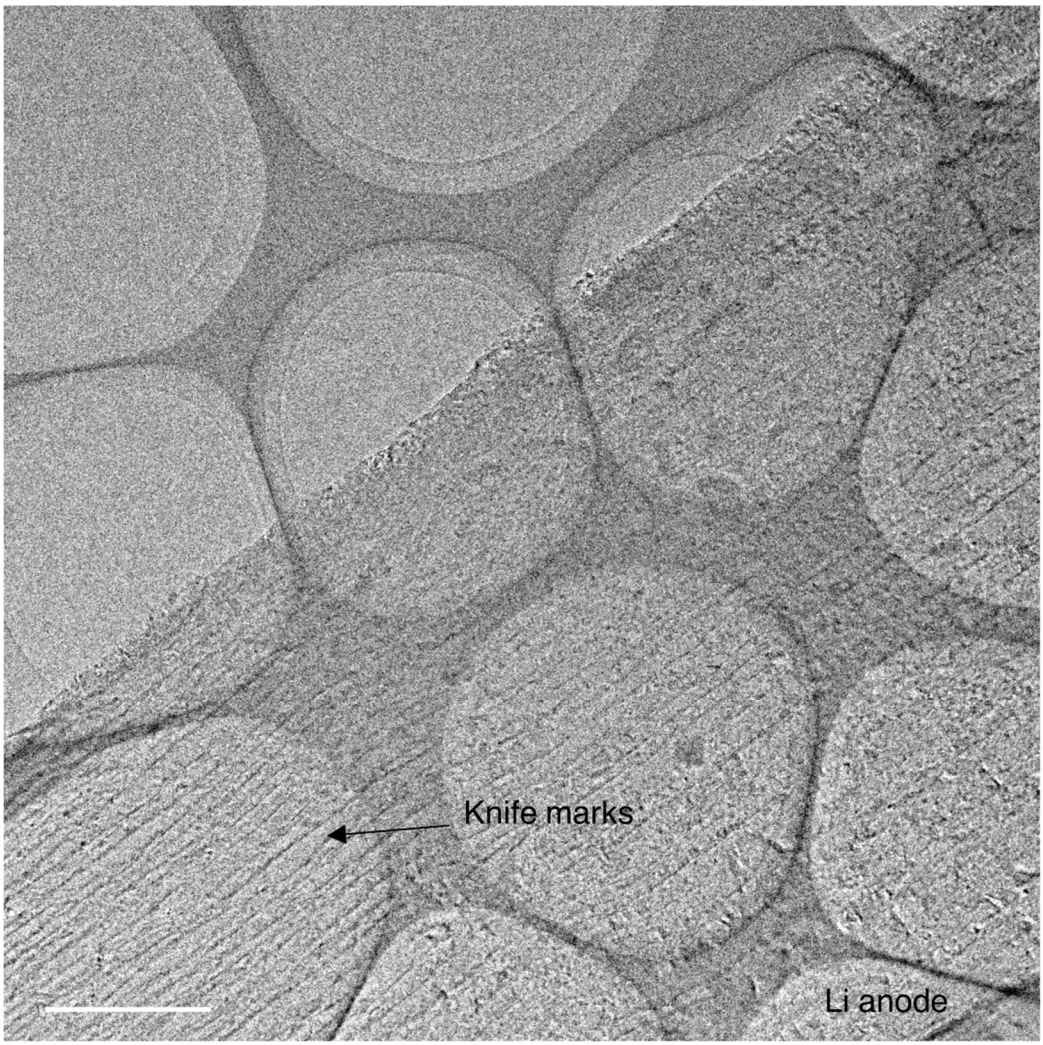

Fig. S2 | The Cryo-TEM bright-field image of the lithium anode, scale bar is 2 μm, showing knife marks on the thin lithium slice.

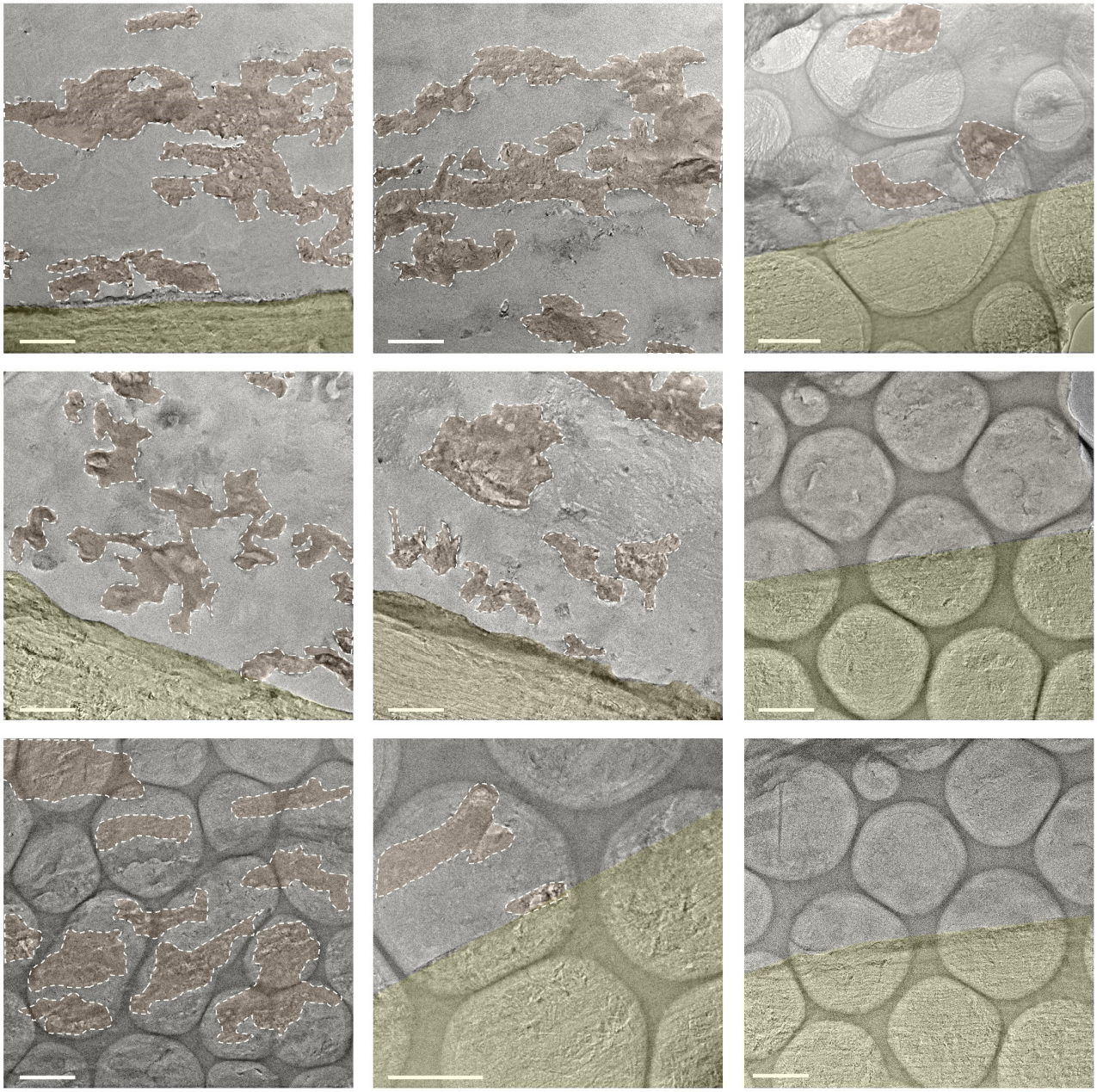

Fig. S3 | Additional Cryo-TEM bright-field images of the Li-PEO interface. Repetitive sectioning procedures were executed to consistently cut ultrathin Li-PEO interface slices (color-enhanced), where the light gray region represents PEO electrolyte, the brown region indicates dendrites (white dashed outline), and the yellow area corresponds to the lithium negative electrode. scale bar 2 μm.

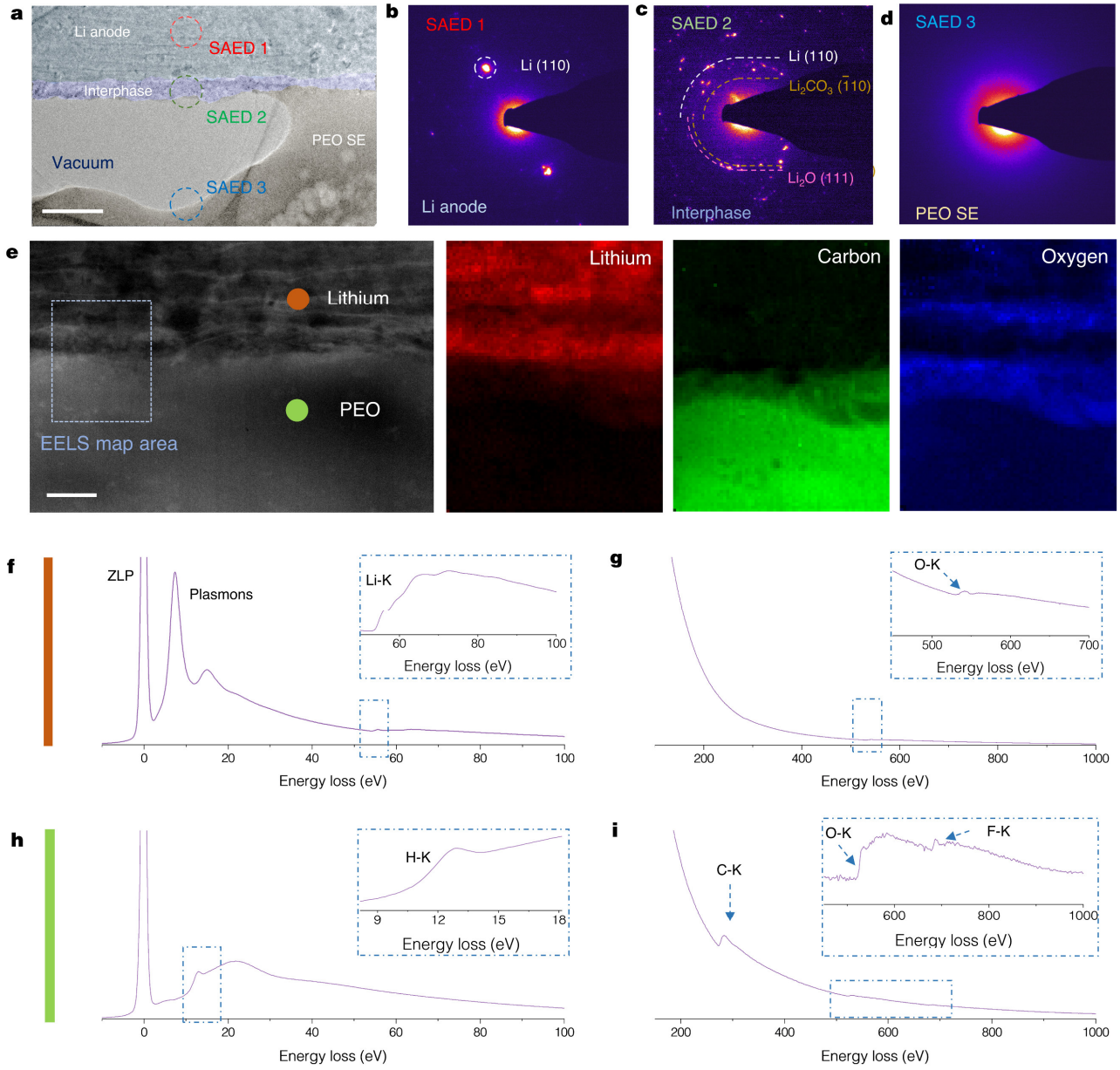

Fig. S4 | Diffraction and EELS characterization of lithium anode and PEO electrolyte after soft short-circuiting. a-d, a Bright-field image at the Li-PEO interface (color-enhanced) along with SAED. Scale bar, 0.5 μm. SAED 1 illustrates the diffraction pattern arising from the lithium anode, distinctly revealing the (110) facet of metallic lithium (**b**). SAED 2 corresponds to interface diffraction, displaying evident polycrystalline patterns attributable to Li, Li_2O, and Li_2CO_3 species (**c**). SAED 3 portrays diffraction patterns resulting from the PEO electrolyte, manifesting as a diffuse amorphous ring (**d**). **e,** ADF image of the interface and EELS map, wherein dark shading designates the presence of lithium. Scale bar, 0.5 μm. The interface exhibits an enrichment of oxygen species, signifying the reaction between PEO and lithium at the interface; **f, g,** Lithium anode's low-loss spectrum (**f**) and core-loss spectrum (**g**), featuring sampling points as indicated in b. The low-loss region notably exhibits plasmon peaks intrinsic to lithium metal (7.52 eV), coupled with the characteristic K-edge signature of metallic lithium. A subtle oxygen signal is also registered, likely attributed to trace oxygen within the electron microscope chamber; **h, i,** Low-loss spectrum (**h**) and core-loss spectrum (**i**) of the PEO electrolyte are illustrated, with sample points corresponding to b. Discernible features encompass PEO's H-K edge (13 eV), C-K edge (284 eV), and O-K edge (532 eV), in addition to the F-K edge (685 eV) characteristic of lithium salt.

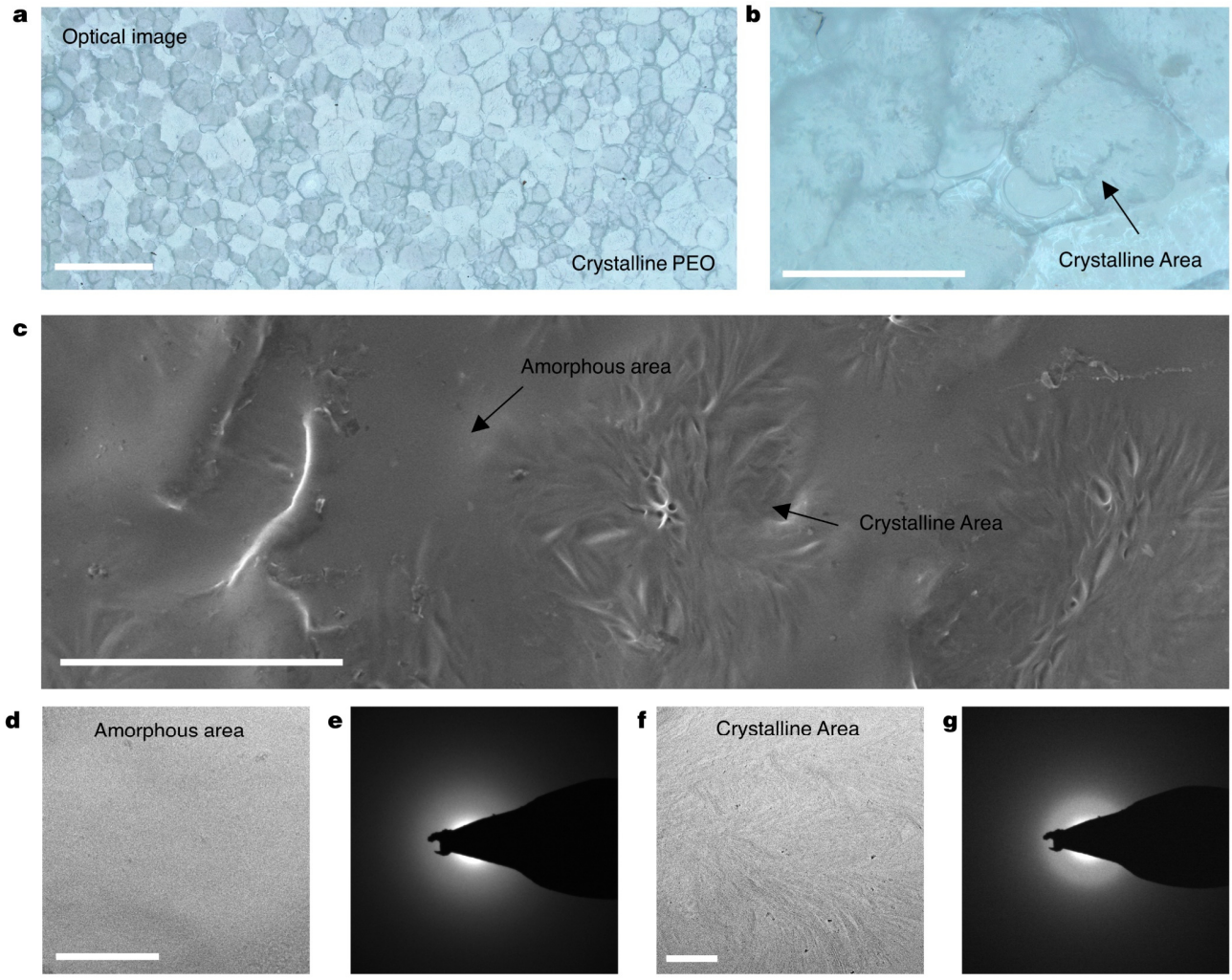

Fig. S5 | Multi-scale characterization of crystalline and amorphous PEO. a, Room-temperature optical microscopy characterization of SPEs crystalline region. Dark areas represent crystalline regions, scale bar 0.1 mm; **b**, Magnified image of the crystalline region, scale bar 20 μm; **c**, SEM imaging of PEO. PEO crystals present spherical morphologies with sizes of 10-20 μm, while the amorphous regions exhibit uniform contrast. Scale bar is 20 μm; **d-g**, Cryo-TEM bright-field images of PEO after cryo-sectioning (**d**). The amorphous PEO areas exhibit a smooth and uniform contrast (**d**) with the corresponding EDP exhibits a broad amorphous halo (**e**). The crystalline regions have fiber-like contrast (**f**), whose EDP also shows diffuse halo (**g**), scale bar 2 μm.

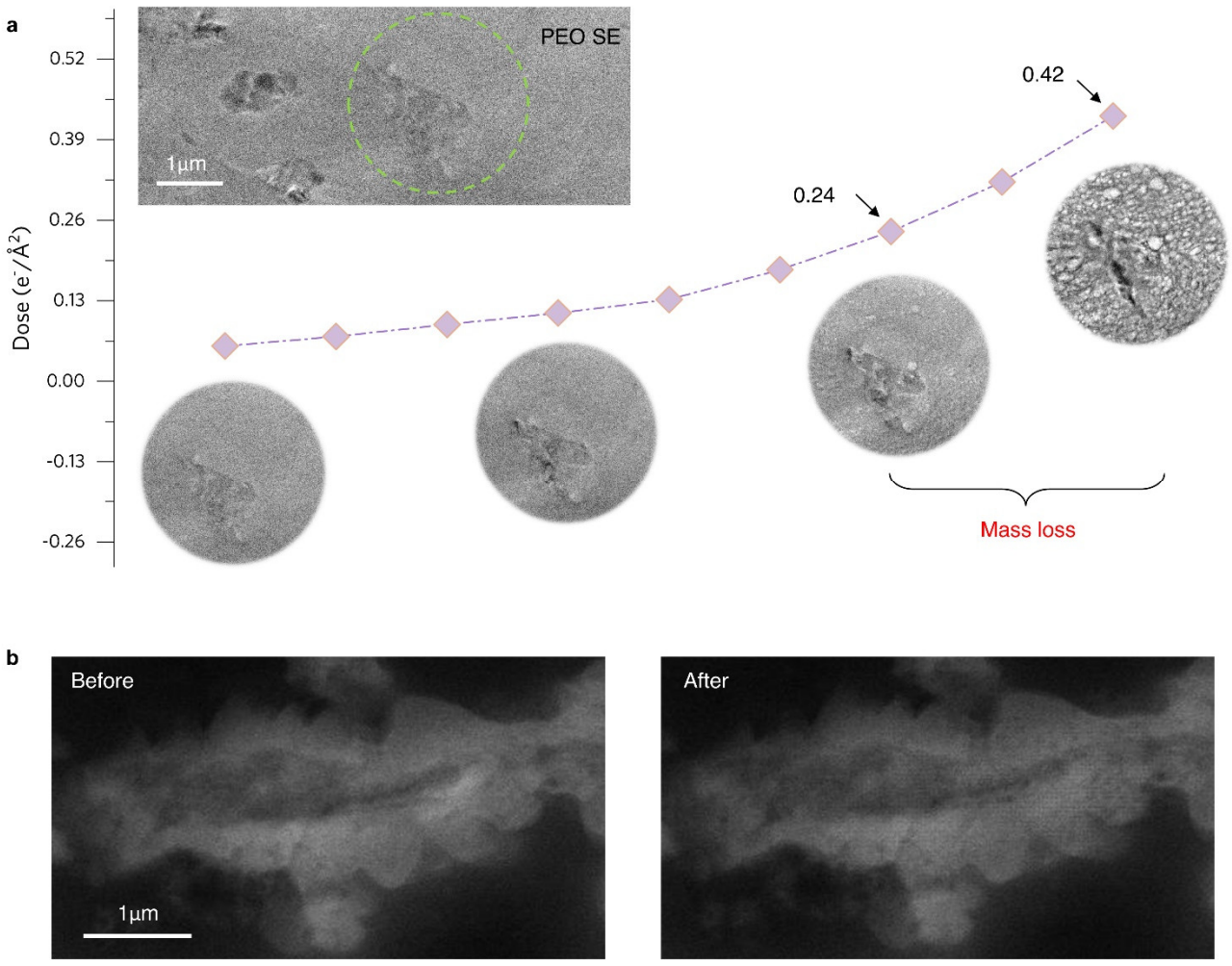

Fig. S6 | PEO Cryo-TEM radiation damage testing. a, Bright-field images of PEO at varying dose levels. Each exposure duration remained constant at 1 s. A noticeable mass loss was observed as the dose surpassed 0.24 $e^-/Å^2$. **b**, ADF images before and after EELS map acquisition for the region shown in Fig. 3a. No discernible sample damage occurred during the process.

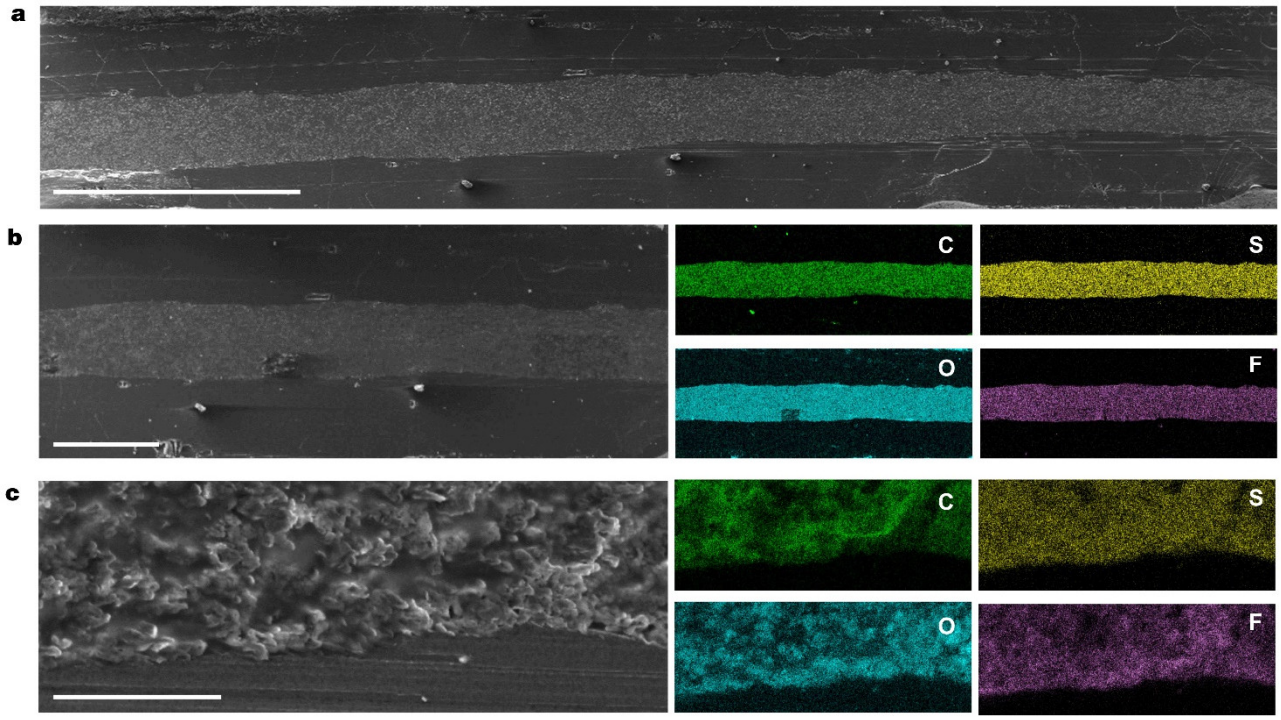

Fig. S7 | SEM and EDX mapping characterization of Cryo-polished Li||SPEs||Li symmetric battery. a, Large area view of the battery cross-section, with lithium metal on top and bottom, and a PEO electrolyte layer in between. scale bar 0.5 mm; **b,** EDX mapping characterization of the cross-section, capturing C and O signals belonging to PEO, as well as F and S signals belonging to lithium salts. No distinct O signal was observed at the lithium metal region, confirming the absence of contamination during sectioning and transfer. Scale bar 200 μm; **c,** EDX mapping characterization of the Li-PEO interface. Oxygen element shows accumulation at the interface and within the dendritic regions, consistent with Cryo-TEM results. Scale bar 20 μm.

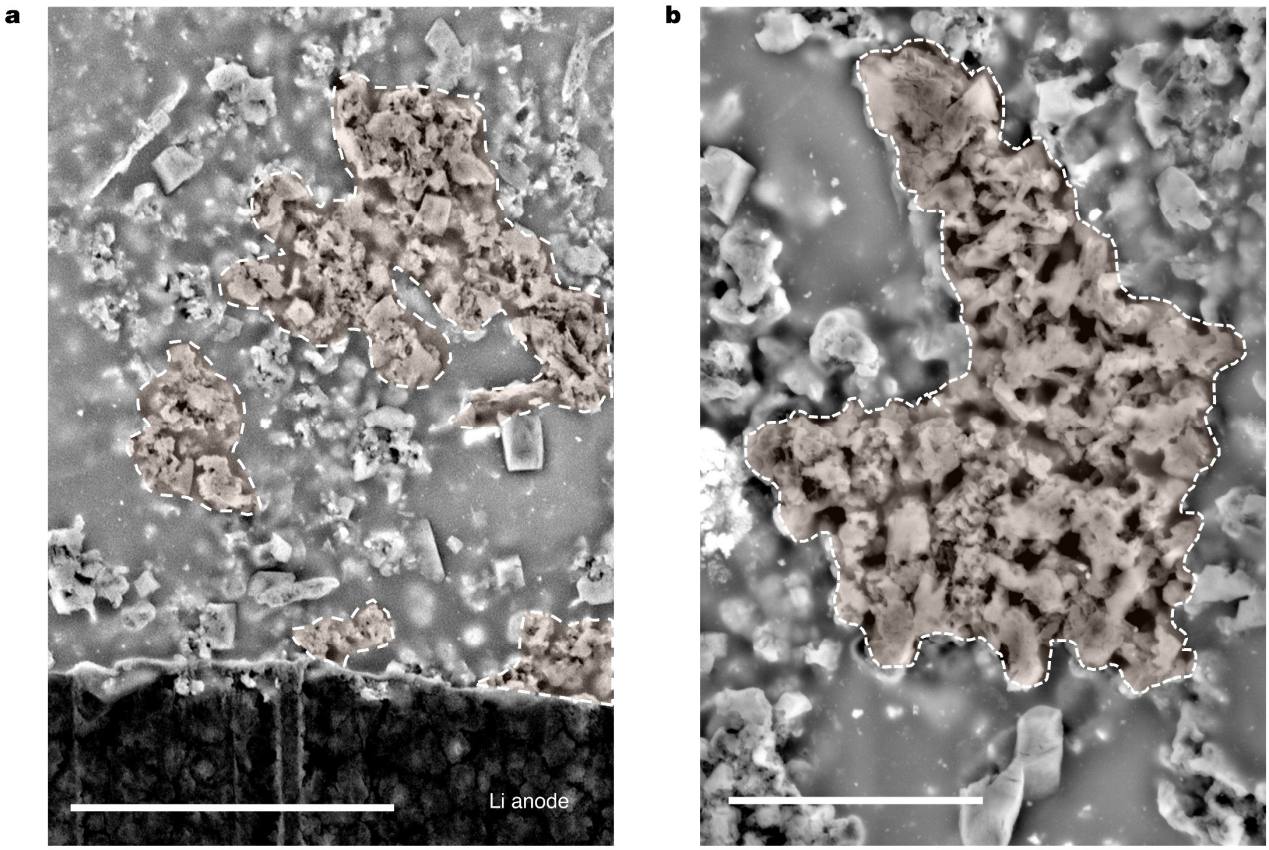

Fig. S8 | The SEM images of dendrite fragments or clusters. a, Image of backscattered electrons on the anode side, with clusters of fragments outlined in white dotted lines. **b,** Clustered lithium inside the SPE**.** Scale bar 20 μm.

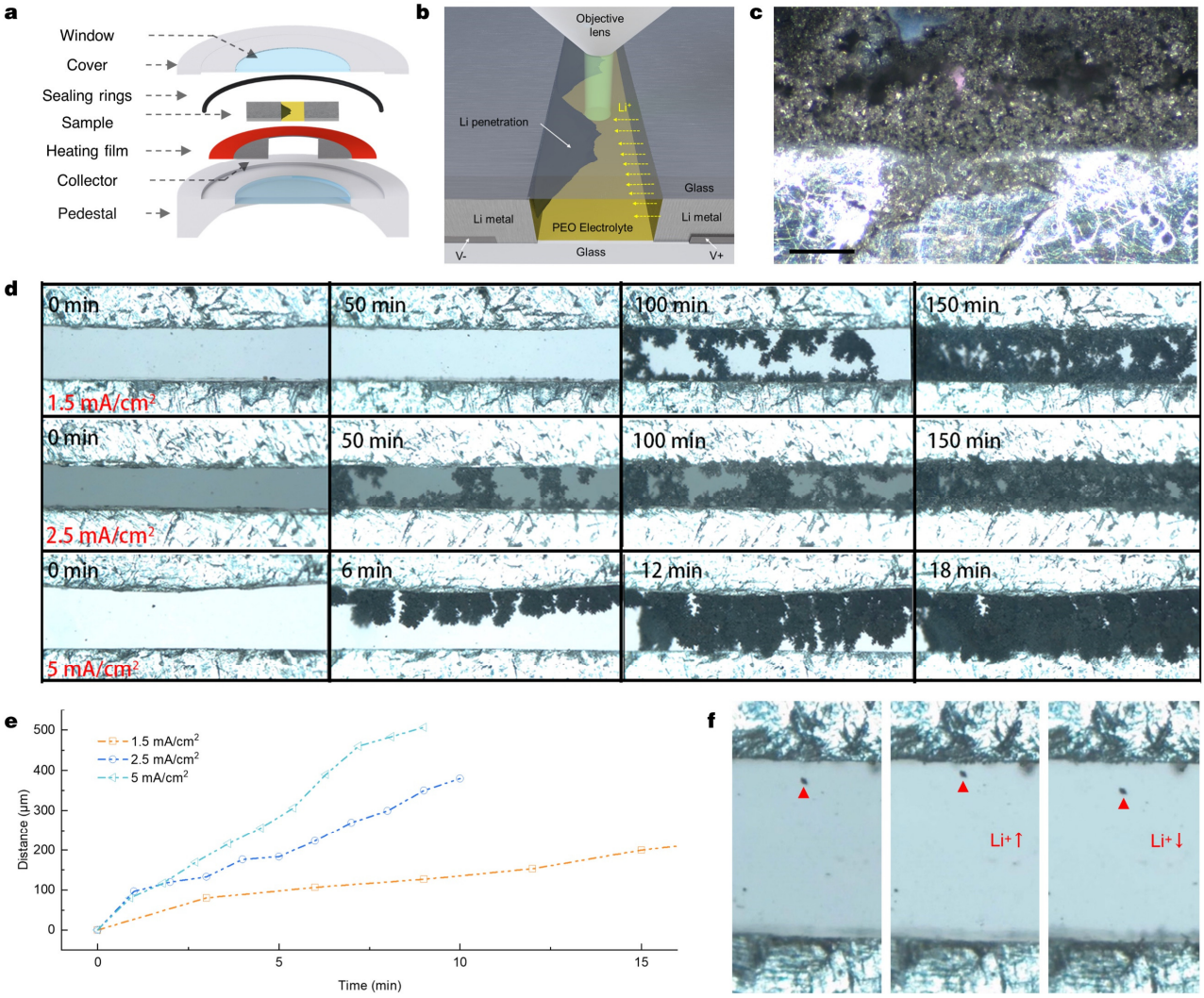

Fig. S9 | In-situ optical setup and real-time monitoring of dendrite growth. a, The schematic portrayal of the in-situ optical setup; **b,** Schematic of the in-situ observations; **c,** Optical image of dendrites at the Li-SPE interface. Scale bar, 100 μm. **d,** Dynamic tracking of dendrite evolution in Li||SPEs||Li symmetric cells at varying current densities. Beyond the 1 mA/cm^2 threshold, dendrites promptly penetrated the PEO layer, inducing short-circuiting. Progressive increments in current density enhance the growth rate; **e,** Analysis of lithium dendrite growth length over time under different current densities within the PEO electrolyte; **f,** The impurities within PEO can be used as marks to track the directional flow of PEO under electric field.

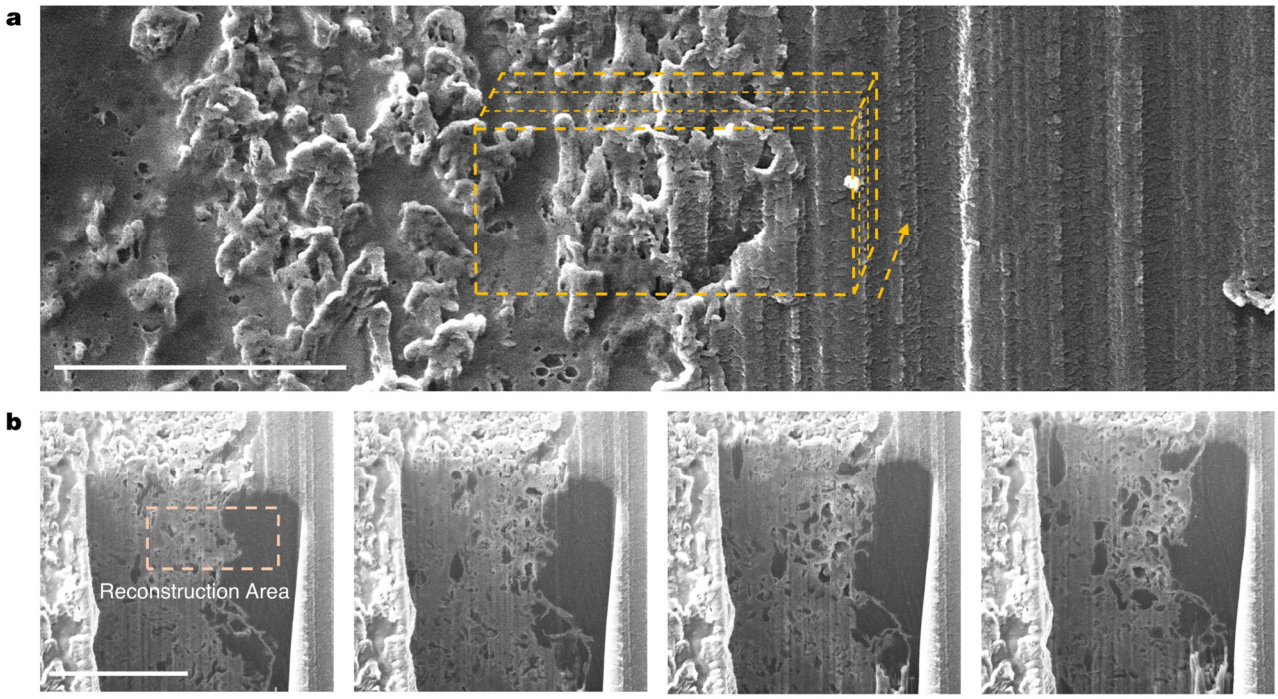

Fig. S10 | FIB-3D reconstruction of dendrites. a, a defined region selected for 3D reconstruction of the Li-PEO interface after soft short-circuiting. The left segment illustrates the PEO and dendrite regions, while the right segment represents the lithium anode area. Scale bar, 10 μm; **b,** cutting profile within the chosen region is illustrated, employing ion beam milling, where lithium exhibits darker contrast. Scale bar, 10 μm;

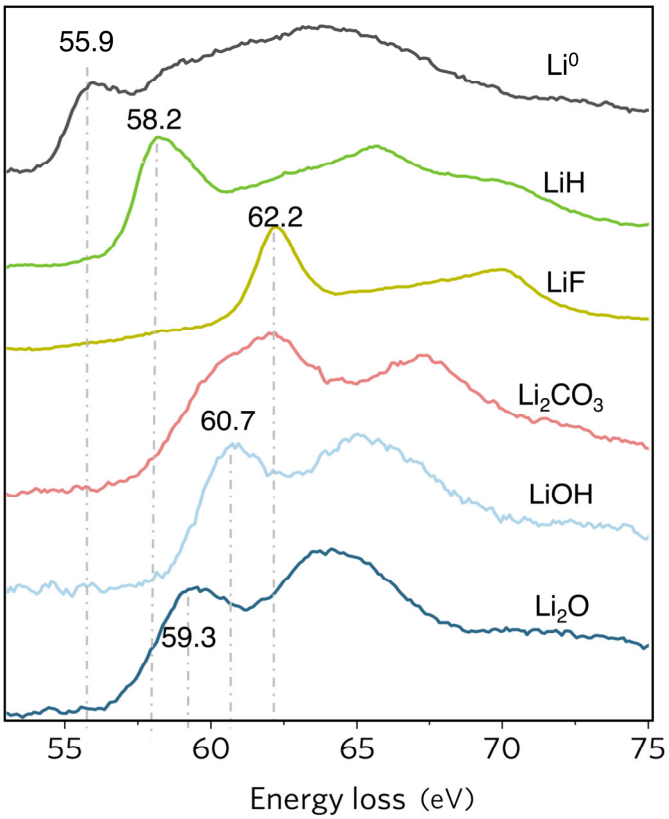

Fig. S11 | Li-K ELNES spectra of different lithium compounds.

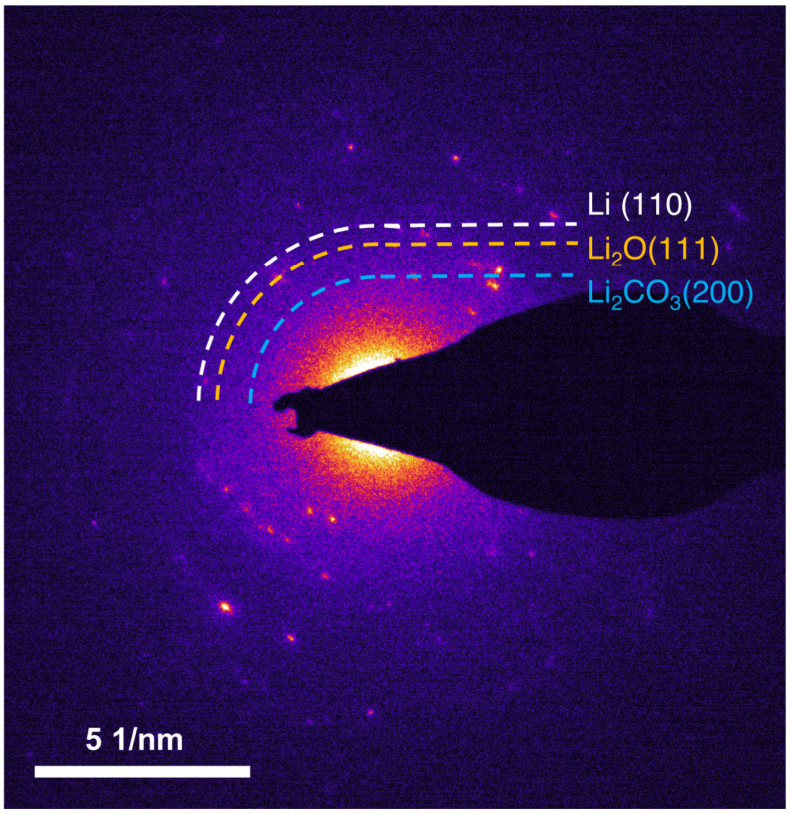

Fig. S12 | The diffraction pattern of the tri-layer structure.

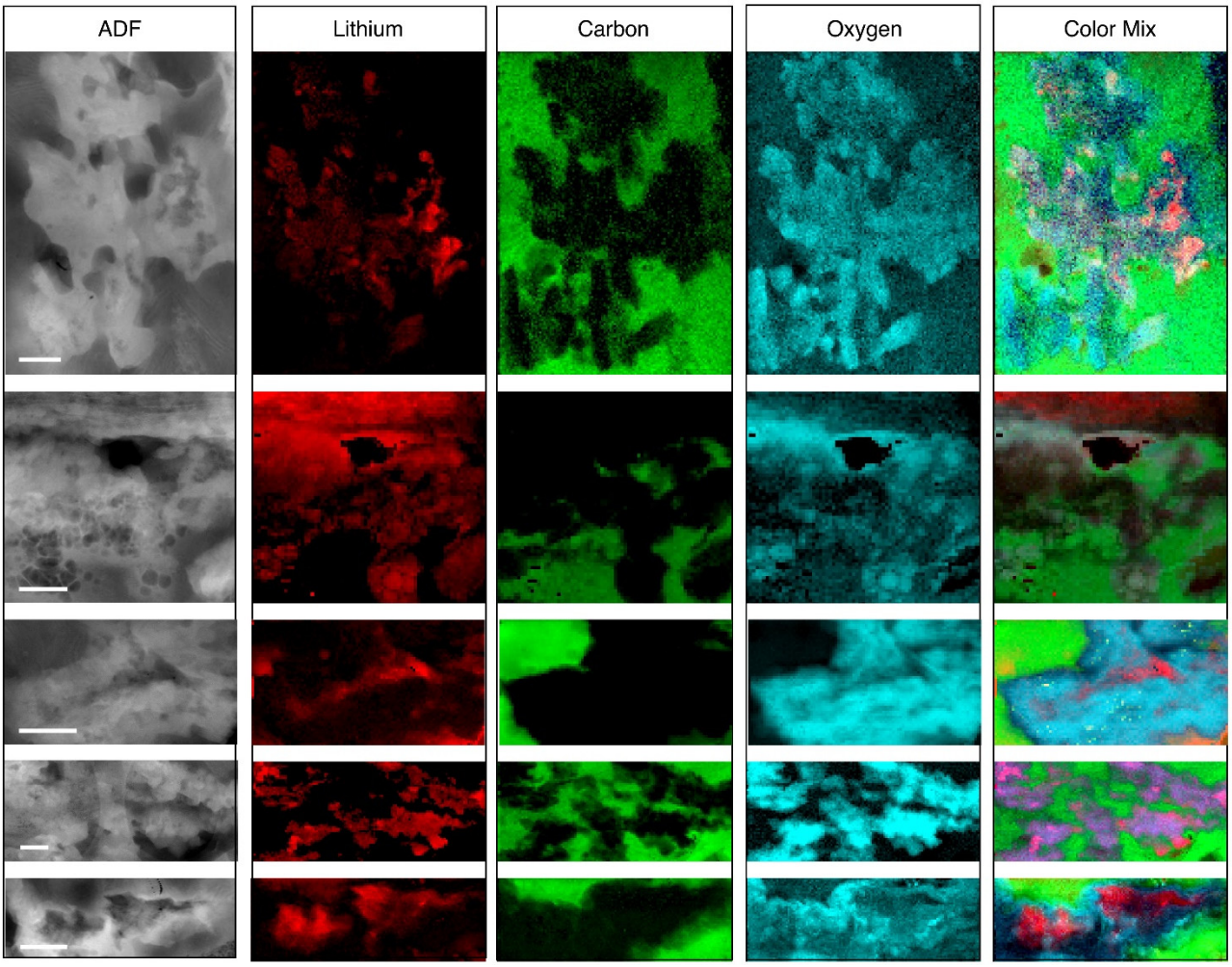

Fig. S13 | EELS elemental mapping of dendritic lithium in different regions. Scale bars 0.5 μm.

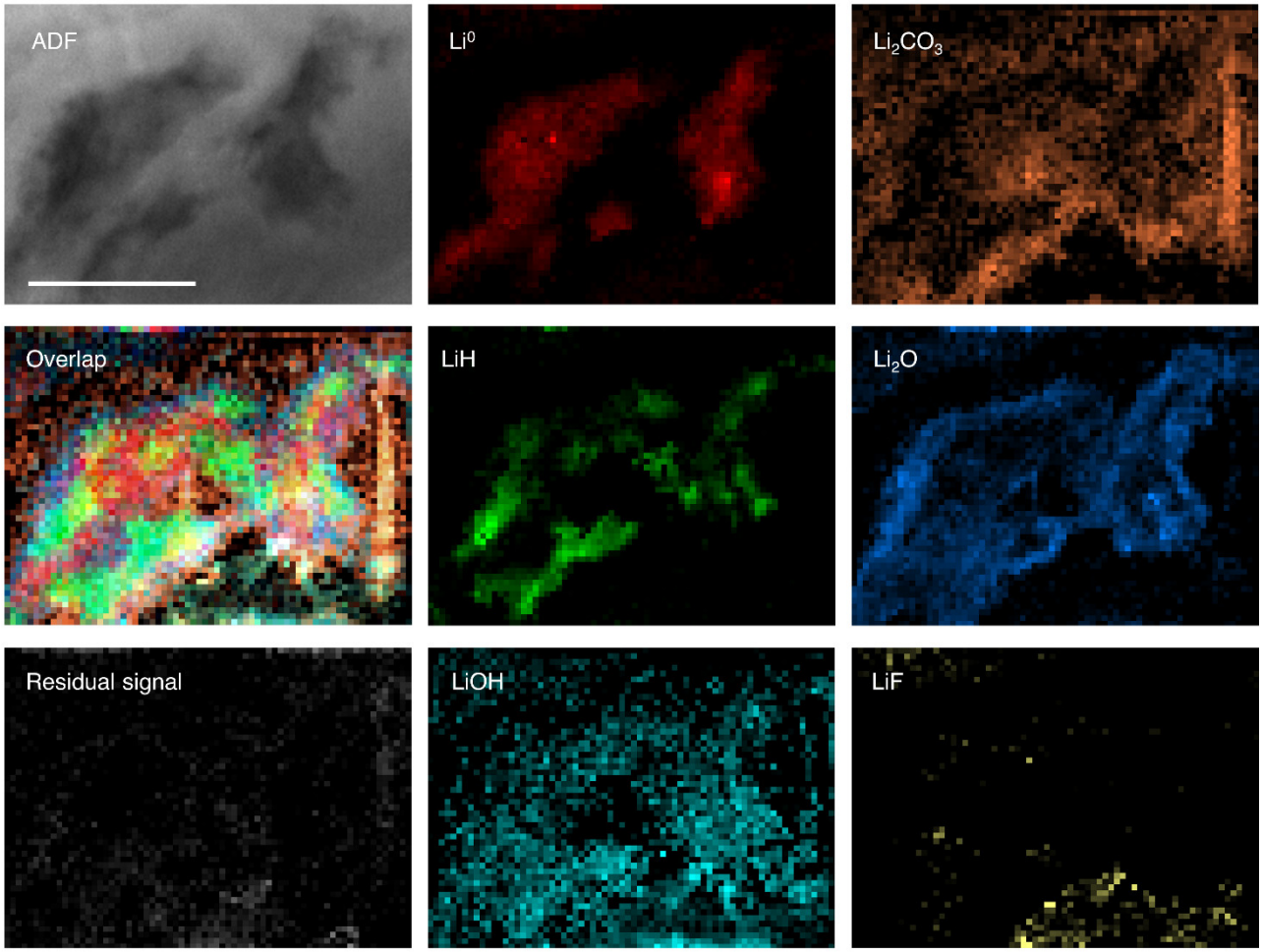

Fig. S14 | EELS-MLLS mapping of additional dendritic lithium region (region 2) under soft short-circuit conditions. Scale bars 0.5 μm.

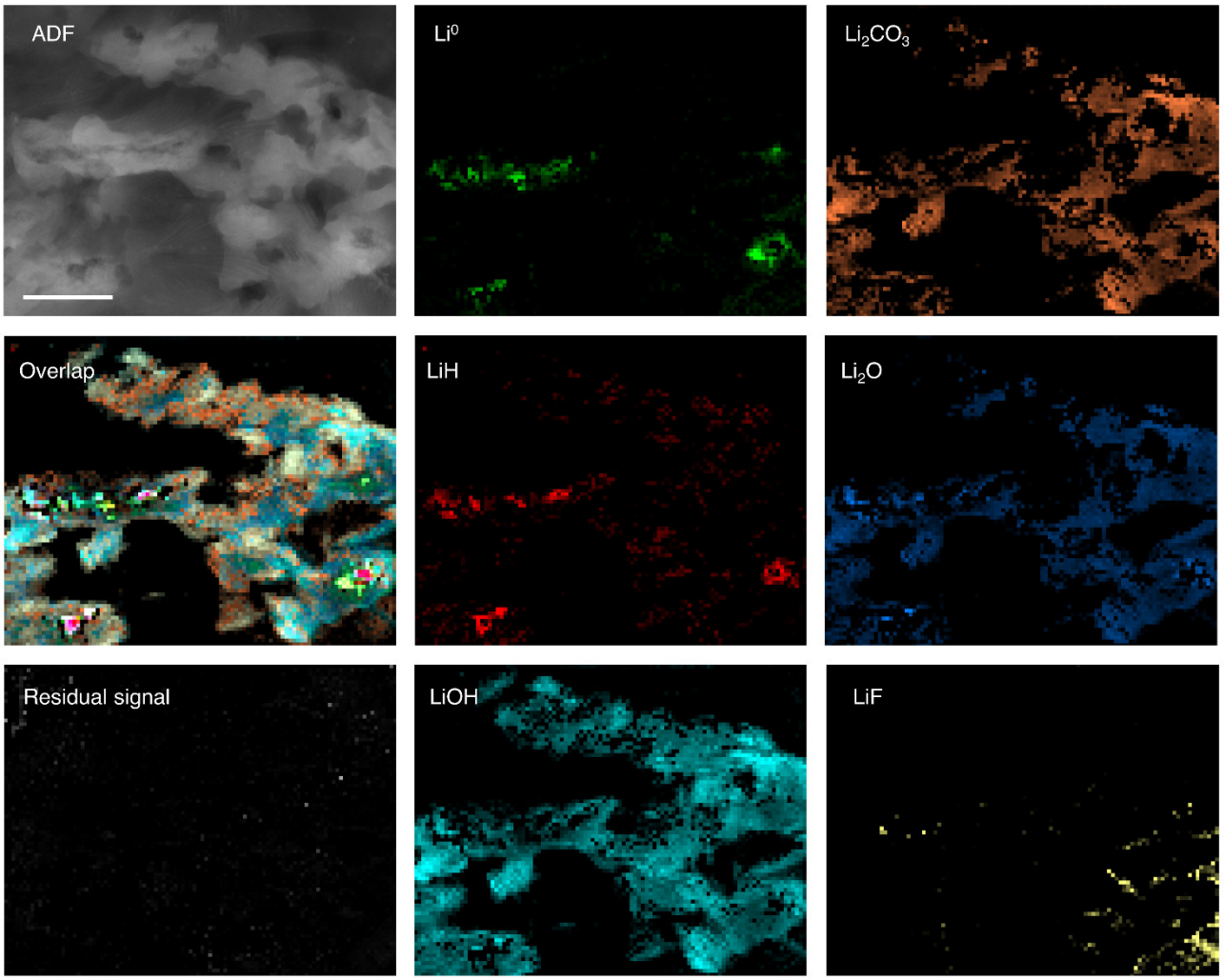

Fig. S15 | EELS-MLLS mapping of additional dendritic lithium region (region 3) under soft short-circuit conditions. Scale bars 2 μm.

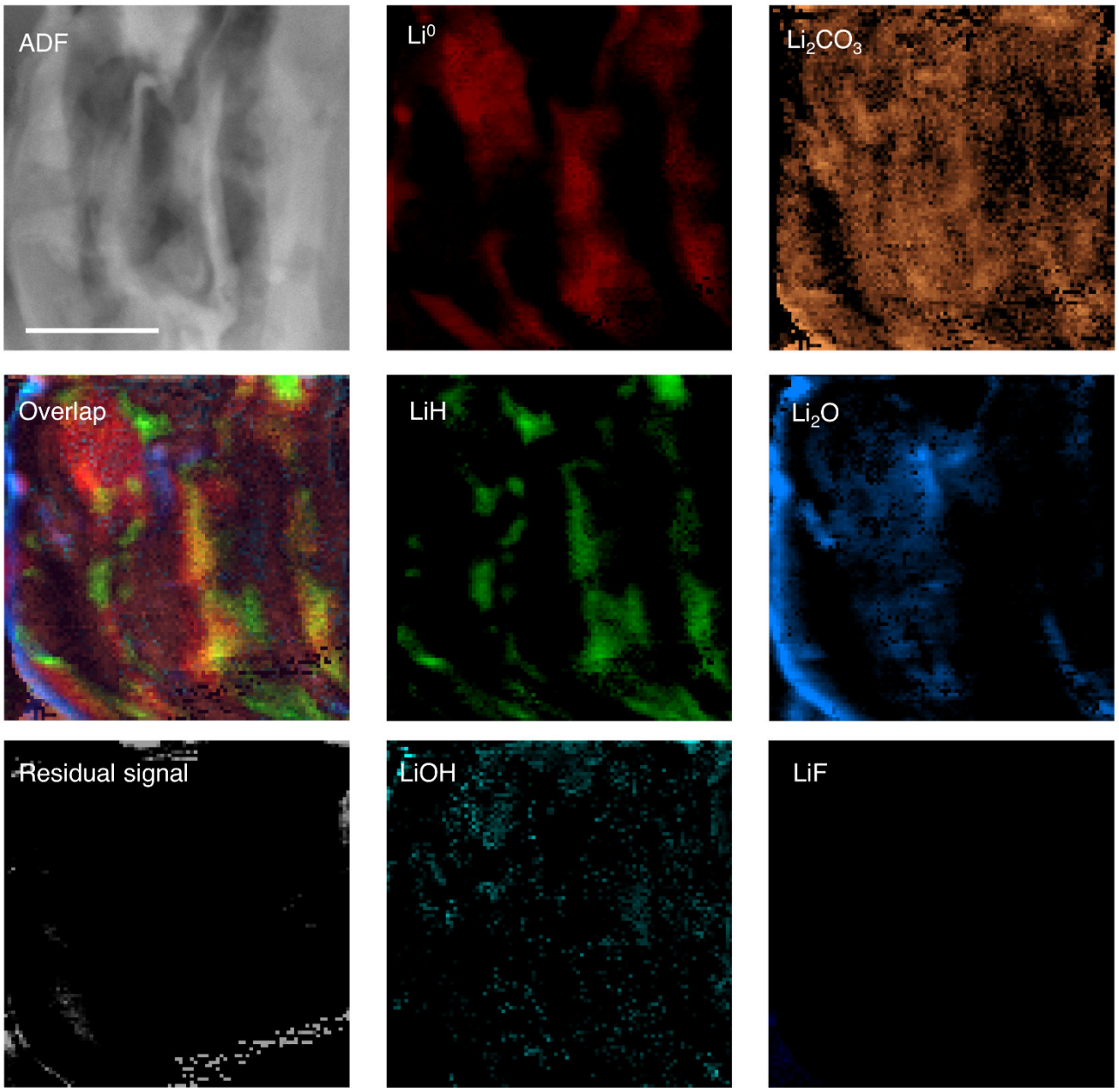

Fig. S16 | EELS-MLLS mapping of additional dendritic lithium region (region 4) under soft short-circuit conditions. Scale bars 0.5 μm.

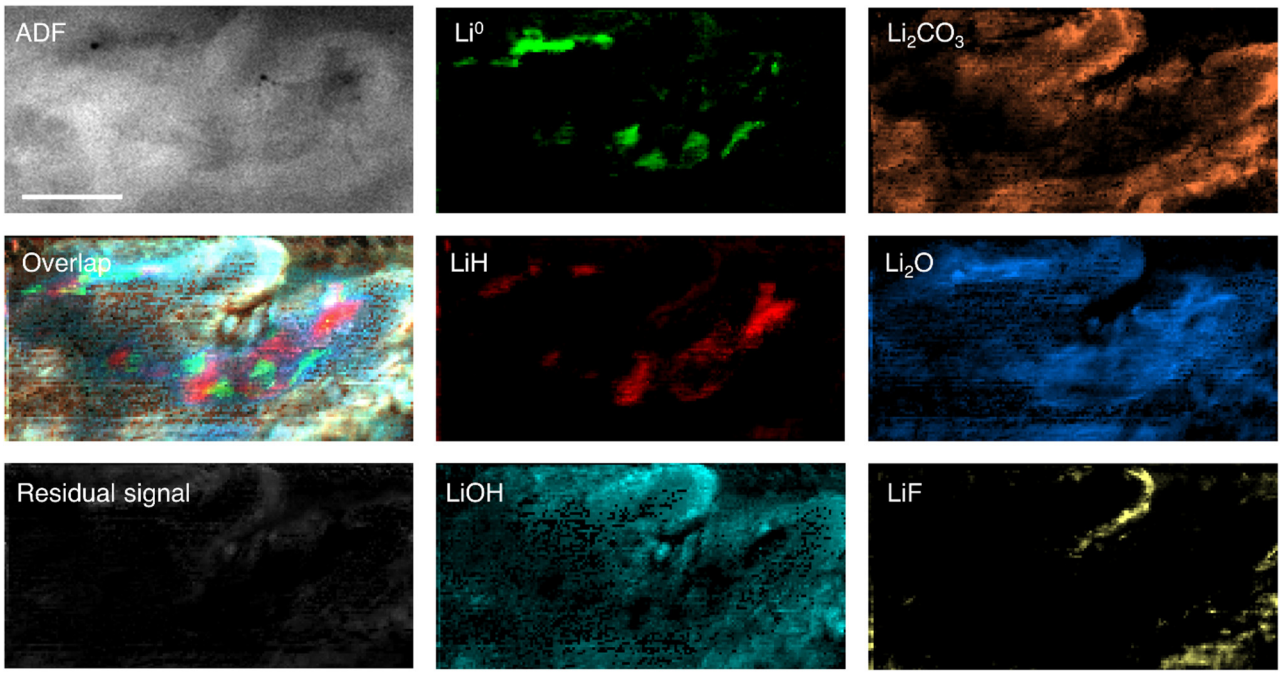

Fig. S17 | EELS-MLLS mapping of additional dendritic lithium region (region 5) under soft short-circuit conditions. Scale bars 0.5 μm.

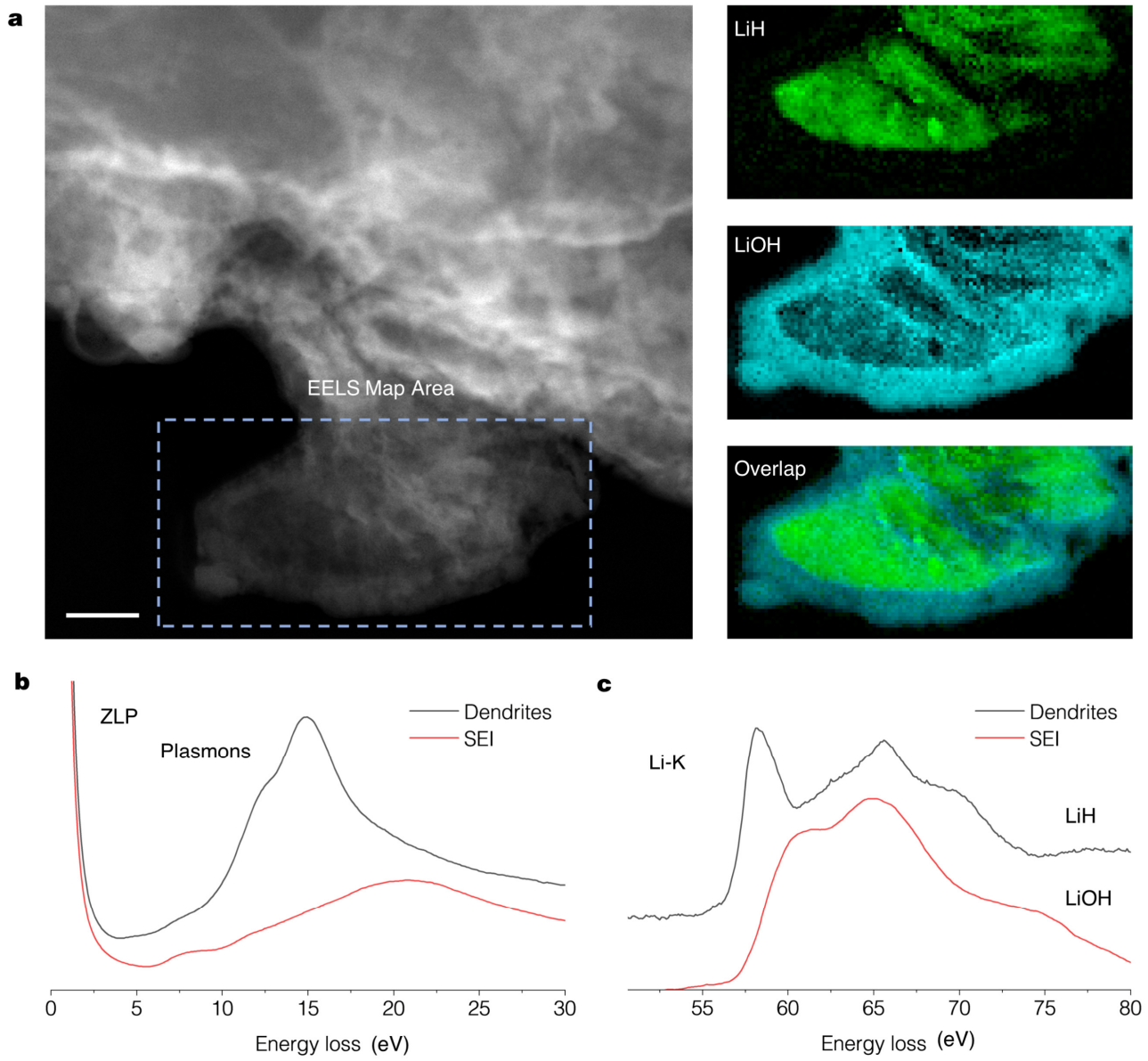

Fig. S18 | EELS validation of LiH presence within the polymer matrix. a, an ADF image of the lithium anode surface, with the acquired EELS map encompassing LiH and its SEI. Scale bar, 0.2 μm; **b, c,** Plasmon peaks (**b**) and the Li-K edge (**c**) of LiH and its SEI, both were extracted from the EELS map in **a**. The conspicuous and characteristic signal of LiH is discernible, accompanied by a concurrent core loss in the SEI with LiOH. This comprehensive spectroscopic analysis demonstrates the presence of LiH within the polymer matrix.

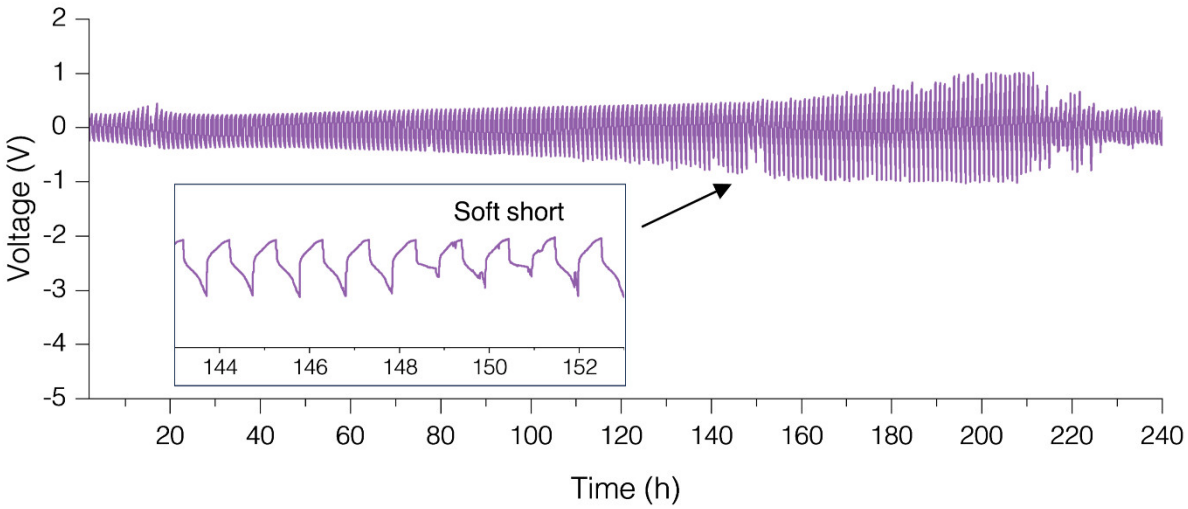

Fig. S19 | Following the incorporation of 5% TBAF, the battery voltage profile. After the short circuit, the battery was used for Cryo-TEM characterization.

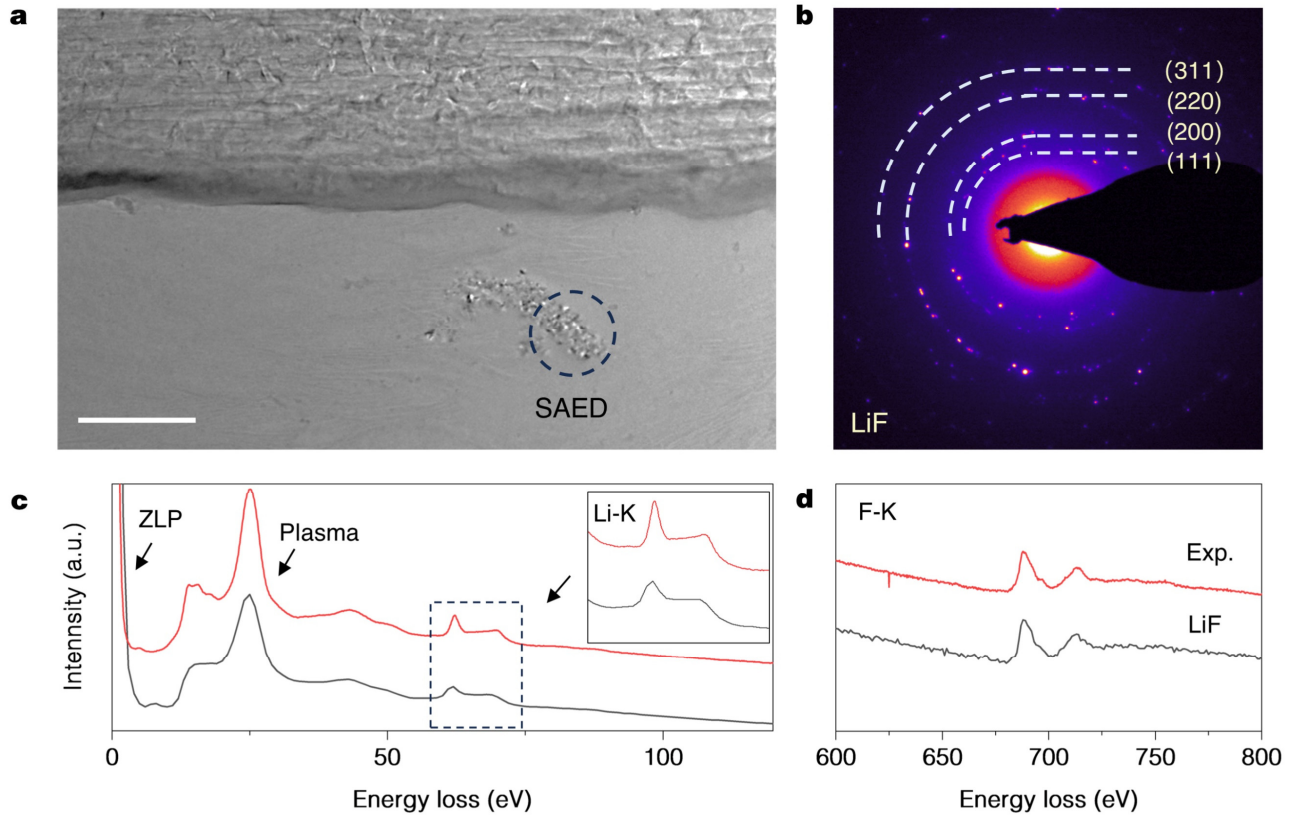

Fig. S20 | Verification of LiF generation after 5% TBAF addition. a, Following the incorporation of 5% TBAF, the Cryo-TEM bright-field image of the negative electrode interface reveals discrete LiF entities. Scale bar, 0.5 μm; **b,** The SAED pattern within the region depicted in **a,** corresponding to the polycrystalline diffraction rings of LiF; **c, d,** EELS low-loss spectrum (**c**) and the F-K edge (**d**) extracted from the region highlighted in **a**. The acquired absorption spectra exhibit a high degree of similarity with those derived from previously characterized standard specimens. This evidence robustly substantiates the LiF formation after the addition of 5% TBAF into the PEO electrolyte.

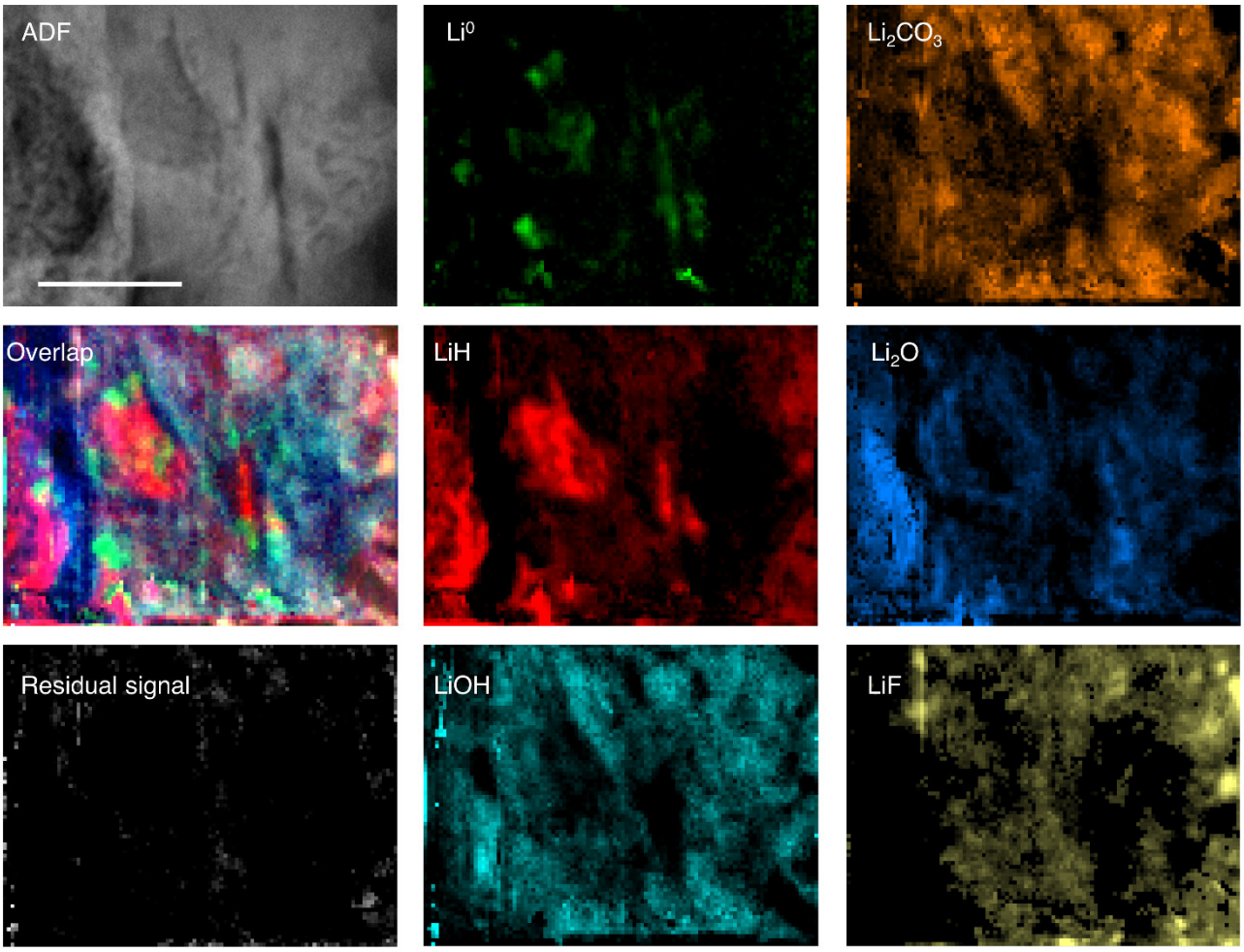

Fig. S21 | Following the introduction of 5% TBAF, EELS-MLLS mapping of additional dendritic lithium region (Region II) under soft short-circuit conditions. Scale bars 0.5 µm.

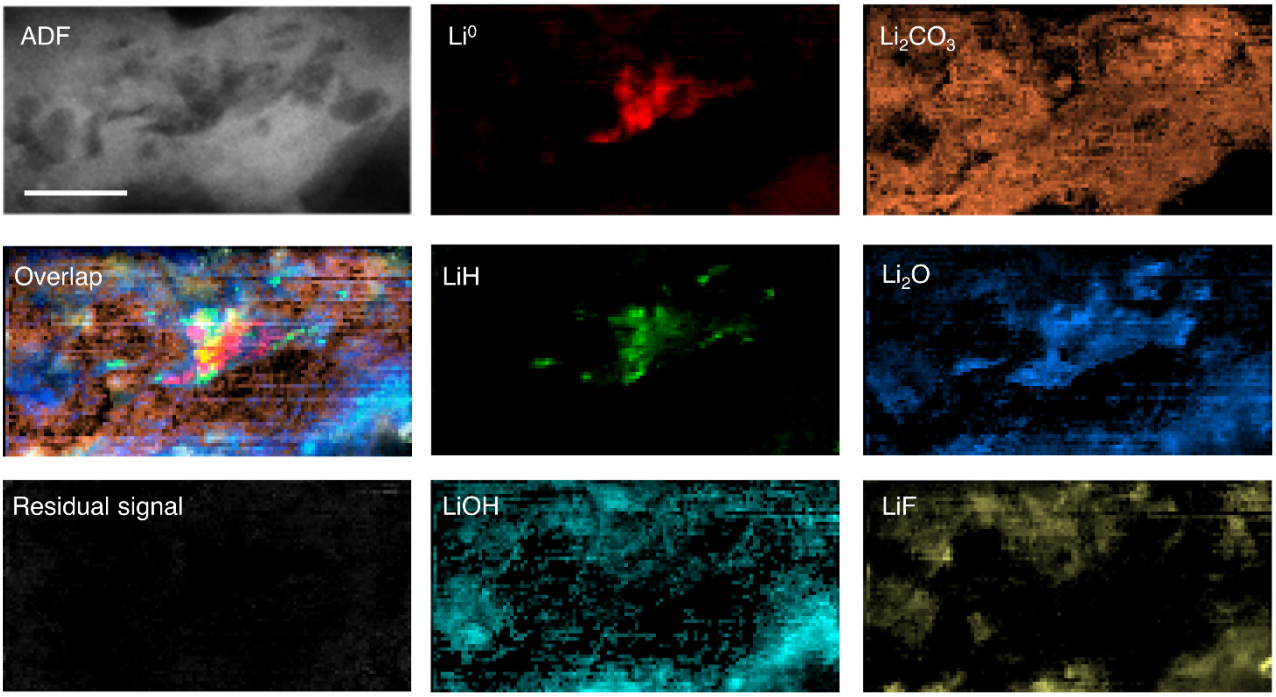

Fig. S22 | Following the introduction of 5% TBAF, EELS-MLLS mapping of additional dendritic lithium region (Region II) under soft short-circuit conditions. Scale bars 0.5 µm.

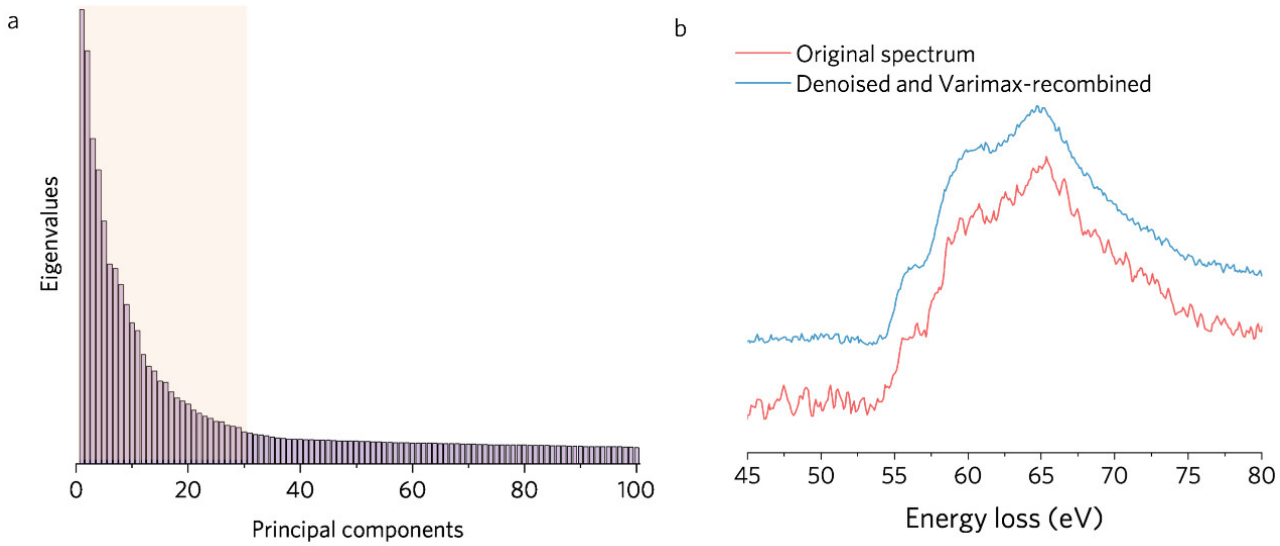

Fig. S23 | After the PCA processing, the top 30 components were selected from the 100 extracted eigenvalues (a). The comparison of Li-K edge spectra before and after noise reduction (b). Initially, we perform zero peak calibration (SI-aligned) on the collected raw data. Subsequently, the SI-aligned data undergoes PCA using Multivariate Statistical Analysis (MSA) provided by Digital Micrograph software, reducing it to 100 feature. The top 30 components are selected for noise reduction. Finally, these 30 features are reintegrated into SI-aligned-recombined,

Supplementary Table

Table S1 Normalized fitting coefficient of SEI components for each region (Region 1 is shown in Fig. 3a; Regions 2-5 are shown in Fig. S14-17, respectively).

	Li_2CO_3	Li_2O	LiOH	LiF	Li	LiH
Region 1	0.0047	0.4344	0.2003	0.0036	0.3354	0.0212
Region 2	0.0998	0.4299	0.0614	0.0235	0.3464	0.0389
Region 3	0.1468	0.2386	0.1510	0.0246	0.0604	0.3785
Region 4	0.2003	0.0597	0.6432	0.0499	0.0159	0.0310
Region 5	0.0559	0.179	0.5740	0.0450	0.1069	0.0390
average value	**0.1015**	**0.2683**	**0.3260**	**0.0293**	**0.1730**	**0.1017**

Table S2 Following the introduction of 5% TBAF, the normalized fitting coefficient of SEI components for each region (Region I is shown in Fig. 4a; Regions II and III are shown in Fig. S21,22).

	Li_2CO_3	Li_2O	LiOH	LiF	Li	LiH
Region I	0.0577	0.1236	0.3921	0.1266	0.2484	0.0515
Region II	0.3194	0.2229	0.2165	0.1344	0.0903	0.016
Region III	0.1923	0.2858	0.2584	0.1060	0.1289	0.0284
average value	**0.1898**	**0.2108**	**0.2890**	**0.1223**	**0.1559**	**0.0321**

Reference

1. K. Richter, *Micron*, 1994, **25**, 297-308.
2. Studer and Gnaegi, *Journal of Microscopy*, 2000, **197**, 94-100.